inventions

Article

Evaluation of a Serrated Edge to Mitigate the Adverse Effects of a Backward-Facing Step on an Airfoil

Real J. KC [1], Trevor C. Wilson [1], Aaron S. Alexander [2], Jamey D. Jacob [1], Nicholas A. Lucido [3] and Brian R. Elbing [1,*]

[1] Mechanical and Aerospace Engineering, Oklahoma State University, Stillwater, OK 74078, USA; realk@okstate.edu (R.J.K.); trevor.wilson@okstate.edu (T.C.W.); jdjacob@okstate.edu (J.D.J.)
[2] Mechanical Engineering Technology, Oklahoma State University, Stillwater, OK 74078, USA; aaral@okstate.edu
[3] Mechanical Engineering, University of Michigan, Ann Arbor, MI 48109, USA; nalucido@umich.edu
* Correspondence: elbing@okstate.edu

Abstract: Backward-facing steps are commonly formed on wings and blades due to misalignment between segments or the addition of protective films. A backward-facing step (BFS) is known to degrade the airfoil performance. To mitigate these adverse effects, a three-dimensional low-profile serrated pattern (termed sBFS) was applied downstream of a BFS on an LA203A profile airfoil. The model drag was determined from wake surveys using a traversing Pitot-static probe within a subsonic wind tunnel operating at a chord-based Reynolds number of 300,000. The airfoil spanned the wind tunnel width (914 mm) and had a 197 mm chord length. Four different sBFS configurations were tested, each formed by applying a 1 mm thick film around the model leading edge. In addition, a BFS at various chord locations and a clean wing (i.e., no film applied) were tested for reference. The sBFS was able to reduce the drag relative the BFS by up to 8–10%, though not outperforming the clean wing configuration. In addition, the wake surveys showed the sBFS produced strong coherent structures that persist into the far-wake region (five chord length downstream of the model) with a scale that was much larger than the step height. Additionally, a computational study was carried out to further examine the flow behavior on the airfoil that produced the coherent structures. This showed that fluid near the surface gets entrained towards the sBFS downstream tip of the sBFS, which creates the initial rotation of these coherent structures that persist into the far-wake region.

Keywords: flow control; backward-facing step; passive; coherent structures; airfoil; drag

Citation: KC, R.J.; Wilson, T.C.; Alexander, A.S.; Jacob, J.D.; Lucido, N.A.; Elbing, B.R. Evaluation of a Serrated Edge to Mitigate the Adverse Effects of a Backward-Facing Step on an Airfoil. *Inventions* **2023**, *8*, 160. https://doi.org/10.3390/inventions8060160

Academic Editors: Peng Du, Haibao Hu and Xiaopeng Chen

Received: 30 October 2023
Revised: 13 December 2023
Accepted: 16 December 2023
Published: 18 December 2023

1. Introduction

A portion of the parasitic drag on an aircraft is due to irregularities and deviations from a smooth (clean) external surface. This contribution is commonly termed excrescence drag. The percentage of the total drag due to excrescence drag varies significantly based on the plane design, size, and operation. The study of surface imperfections dates back to the 1930s (e.g., [1]) and a review of early studies is provided in Young and Paterson [2]. More recently, studies have been performed to better understand excrescence effects on transition and the use of flow-control techniques to mitigate their impact [3–6]. A common source of excrescence drag is the creation of a step due to a mismatch in height between two surfaces. Steps are frequently formed at skin joints, around windows, and control surfaces. In addition, a backward-facing step (BFS) is frequently created when protective films are added to the leading edge of airfoils for various applications including wind turbine and helicopter blades. While these protective films do protect the integrity of the leading edge, the backward-facing step created by the film is detrimental to the performance [7–9]. The issue of a backward-facing step on airfoils is not new and has been studied extensively [10–13]. The current study is a preliminary examination of a serrated (i.e., saw-tooth) pattern being added to the downstream edge of a BFS as a means of mitigating its adverse effects on airfoil aerodynamic performance.

Before the previous study on the sBFS is presented, low-profile flow-control methods will be discussed. A common passive flow-control device is a vortex generator (VG), which is commonly used on aircraft to control the wing aerodynamic boundary layer. It does so by re-energizing the boundary layer to delay flow separation and aerodynamic stalling [14]. Some VGs are designed for specific flow regimes. For example, Yao et al. show that low-profile vortex generators outperform traditional VGs at high angles of attack [15]. The Gurney flap can significantly increase lift at low angles of attack without any penalty in terms of drag [16]. While the advantages of VGs are plenty, passive flow-control methods such as these require tuning of the geometry with the flow conditions, typically resulting in a relatively narrow range where they are beneficial, which is why they are generally designed for specific flow regimes. An extensive review of low-profile VGs is presented by Lin [17]. Additionally, the micro vortex generators that are used in supersonic regimes improve shockwave-induced boundary layer separation [18], or to eliminate the flap separation of take-off and landing configurations of aircrafts and increase the lift-to-drag ratio at various angles of attack [19]. Since these micro VGs are mostly used in supersonic regimes, the literature on subsonic regimes is scarce.

There is evidence that the addition of various patterns to the trailing edge of a BFS is an effective passive flow-control technique for mitigating the adverse effects (e.g., [20]) and even reduction in noise [21]. Serration (i.e., making a saw-tooth pattern) in the BFS is a pattern that has shown potential for mitigating the BFS impact. For the current study, a serrated BFS (sBFS) was created by applying a thin film around the leading edge of an airfoil and then cutting triangular shapes into the downstream edge that would form the BFS. This mimics the use of protective leading edge tapes or coatings used for helicopter and wind turbine blades. Protective tapes without the serration have previously been studied and shown to protect the rotor blades while significantly increasing the profile drag [22]. Qualitative investigations adding the serration suggested that it could mitigate the added drag. The National Renewable Energy Laboratory (NREL) performed a comparative study of the performance of wind turbines with a serrated protective film relative to a non-serrated protective film [23]. The turbine was a two-bladed Westinghouse WWG-0600 with a nominal rotor diameter of 44 m. Preliminary data from that study show the KWH power production increased with the sBFS relative to the BFS by 6% and 7.4% at wind speeds of 7 m/s and 11 m/s, respectively. However, this study only looked at the bulk performance (i.e., turbine efficiency) and no information was provided about the impact of the aerodynamic performance due to the sBFS. Consequently, there is little insight into the relationship between the sBFS shape and flow parameters, which is required to develop an optimized design for a given application.

Most reported aerodynamic work on sBFS has been related to their application on airplane wings. Commercial flight testing with sBFS (termed a conformal vortex generator or CVG) on a Boeing 737 was performed by Safair, which reportedly showed a 1% reduction in fuel consumption [24]. The first assessment of the aerodynamic impact of the sBFS on the Boeing 737 suggested that shock stabilization on the wing could be a cause for the reduced fuel consumption [25]. However, flight tests on a subsonic aircraft (Piper Cherokee) that provided wall shear distribution on the wings indicated that sBFS redistributes the near-wall momentum. This was apparent as a low-shear diamond pattern formed downstream of the sBFS valleys (i.e., the furthest upstream step location) [26]. A computational model was developed to further investigate the induced flow pattern observed on the subsonic aircraft [24]. The model confirmed the low-shear diamond pattern from the subsonic flight tests. Further evaluation computationally [10] and experimentally [26] showed that these diamonds were created by the sBFS peak (i.e., furthest downstream step location), inducing the laminar-to-turbulent transition while delaying the transition downstream of the valley. In addition, these studies showed that low-profile (i.e., step height was approximately 5%

of the boundary layer height) sBFS could produce strong coherent structures that persisted downstream with a height that was comparable to the boundary layer thickness.

The first part of the current study experimentally investigates the sBFS applied to an airfoil (LA203A) mounted in a wind tunnel and operated at subsonic conditions. The aim was to quantify the aerodynamic impact of the sBFS relative to a BFS as well as a clean (i.e., no BFS) wing. The total drag was quantified from wake surveys in the far-wake region. We present evidence that the sBFS-induced coherent structures that persisted into the far-wake region led to further examination of the induced vorticity and its dependence on sBFS size (length and width) for a subset of conditions. All results are compared relative to the BFS and clean conditions. Then, a computational model was created and validated against the available experimental results to further examine the flow behavior on the airfoil that produced the coherent structures. The remainder of the article describes the experimental and computational methods used in Section 2; Section 3 presents drag coefficient and vorticity results from both the experiment and computations; Section 4 provides a qualitative and quantitative discussion of the sBFS's performance; and Section 5 provides a brief summary and concluding remarks.

2. Methods

2.1. Experimental Methods

2.1.1. Test Facility and Model

The experiments were conducted in the custom built Flexible-use Wind Tunnel (Diehl Aero-Nautical) located at Oklahoma State University [27–29]. It was an open loop, draw down tunnel powered with a 125 hp centrifugal fan, which can achieve speeds of up to 30.5 m/s (100 ft/s). The tunnel test section can be varied, and, for the current study, it was 2.44 m (8 ft) long with a 0.91 m (3 ft) square cross section. The freestream turbulent intensity within the test section was measured to be below 1.4% [28]. A schematic of the wind tunnel test section is provided in Figure 1 with the test model located 0.762 m downstream from the test section inlet and vertically centered. The test model was an airfoil with an LA203A profile and a chord length (c) of 0.197 m (7.75 in). The model airfoil angle of attack (defined in Figure 2a) was then varied for a given test speed.

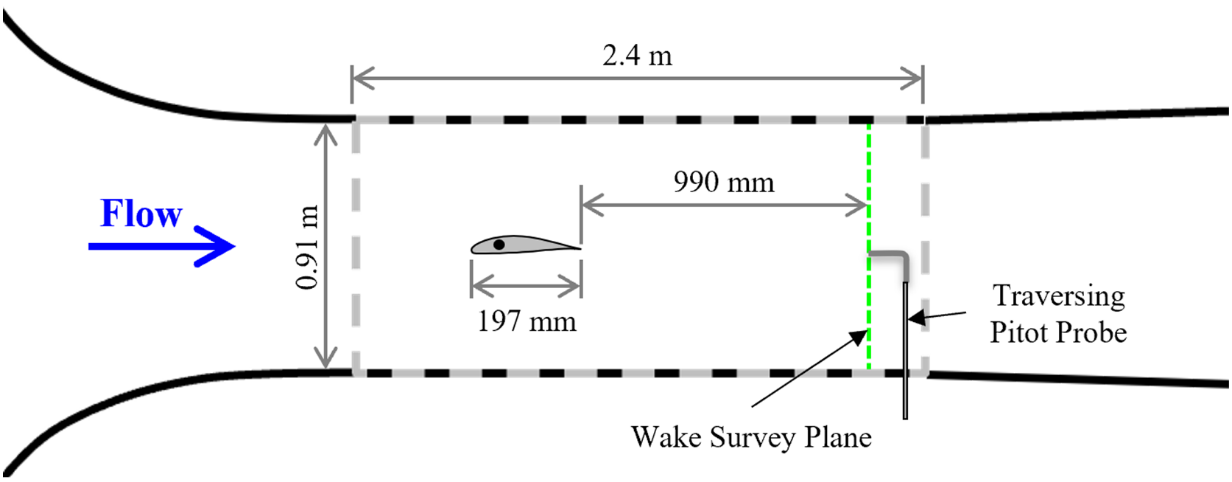

Figure 1. Side view schematic of the wind tunnel test section (dashed rectangle) with the airfoil and probe locations and their relative positions shown.

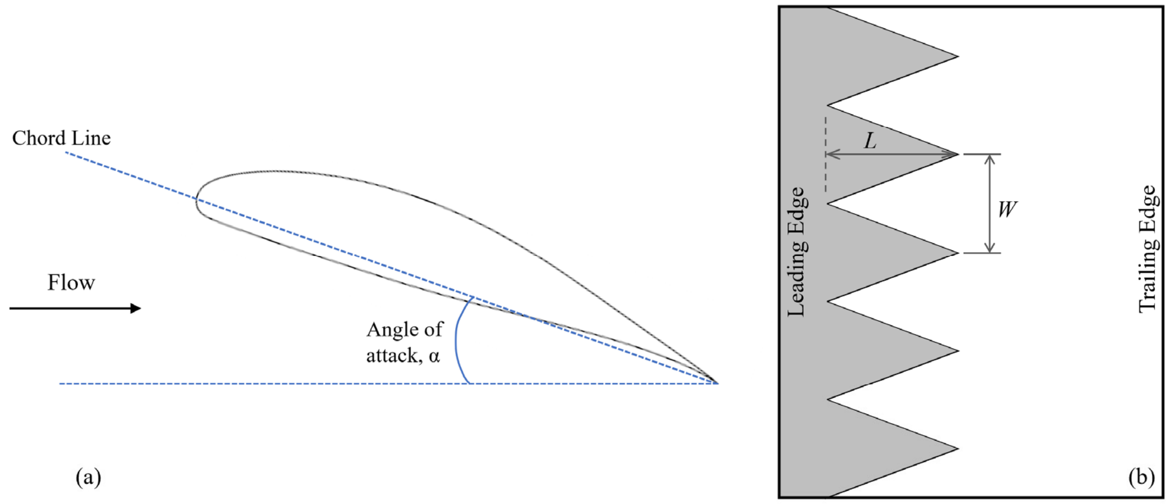

Figure 2. (**a**) The LA203A airfoil profile with the definition of angle of attack (α). (**b**) Schematic of the top view of an sBFS configuration on the airfoil.

2.1.2. Backward-Facing Steps

A film (i.e., thin tape) was applied around the leading edge of the airfoil model and extended downstream to the desired chord location. If a BFS was being tested, the end of the film sheet was cut straight, while for sBFS, a serrated pattern, as illustrated in Figure 2b, would be cut into the film. As previously mentioned, the upstream point and downstream point of the sBFS are referred to as the valley and peak locations, respectively. The height of the BFS and sBFS was fixed at 1.02 mm. The foil thickness varied with a maximum thickness of 15.6% of the chord length (30.7 mm). The step height was selected to correspond to that of a Boeing 737 aircraft following the scaling proposed in Lucido et al. [26], though the current study was subsonic. Four different sBFS configurations were tested, termed sBFS-V1, -V2, -V3, and -V4. The size and position of each sBFS and BFS, as well as their position on the airfoil, are listed in Table 1.

Table 1. Summary of test configurations with the sizes, geometric ratios, and the relative chord positions. NA indicates that the measure is "not applicable."

							Location [%c]	
Model	***L*** **[mm]**	***W*** **[mm]**	***H*** **[mm]**	***L/W***	***L/H***	***W/H***	**Valley**	**Peak**
Clean Wing	NA	NA	NA	NA	NA	NA	NA	NA
BFS1	NA	NA	1.02	NA	NA	NA	10	NA
BFS2	NA	NA	1.02	NA	NA	NA	27.3	NA
BFS3	NA	NA	1.02	NA	NA	NA	44.5	NA
sBFS-V1	70	50	1.02	1.4	68.6	49	10	44.5
sBFS-V2	35	25	1.02	1.4	34.3	24.5	10	27.3
sBFS-V3	35	25	1.02	1.4	34.3	24.5	27.3	44.5
sBFS-V4	70	25	1.02	2.8	68.6	24.5	10	44.5

The sBFS-V1 length (L = 70 mm), width (W = 50 mm), and height (H = 1.02 mm) were three times those tested on the Boeing 737 aircraft, which was selected to scale to flight conditions at cruise altitude [13]. The sBFS-V1 valley was located at 10% chord length as the flight tested on the Boeing 737. To separate geometric and kinematic dependence, the length and width were halved for sBFS-V2, which produced the same L/W ratio without changing boundary thickness or step height. The sBFS-V2 valley location was matched with sBFS-V1 at 10% chord length, but the peak location was changed due to the decreased length. Consequently, sBFS-V3 had the same dimensions as sBFS-V2 but shifted downstream such that its peak location matched the downstream position of sBFS-V1. For the final configuration (sBFS-V4), the length matched that of sBFS-V1, while the width was halved (i.e., matched sBFS-V2 and -V3) to assess the impact of the L/W ratio on the sBFS performance. Both sBFS-V3 and -V4 configurations were tested at the same time with half of the airfoil model span having one of the configurations, which was carried out since initial configurations showed minimal spanwise variation for scales larger than the sBFS width. In addition to the sBFS, the BFS was tested with the step height fixed at 1.02 mm and its location at 10%, 27%, or 44% chord lengths, which corresponds to peak and/or valley locations for the sBFS configurations. Pressure measurements at these locations were not recorded for the experiments; however, they could be tabulated using the simulations. The corresponding pressure gradients were as follows: −8 kPa/m at 10% chord length, 2.5 kPa/m at 27% chord length, and 5 kPa/m at 44% chord length.

2.1.3. Instrumentation and Data Analysis

The primary measurements for the current study were wake surveys via a Pitot-static tube mounted five chord lengths downstream of the airfoil model (see Figure 1). The Pitot-static probe was traversed through the test section cross-section on an automated traverse (Dantec) with each wake survey acquiring data at nominally 100 locations. For all conditions, the streamwise velocity component (u) was measured, and for a subset of conditions, a 5-hole probe was installed. The 5-hole probe measures the velocity magnitude (V), angle of attack (α), and the slip angle (β), which can be converted to the streamwise $(u = V\cos\alpha\ \cos\beta)$, spanwise $(v = V\sin\beta)$, and vertical $(w = V\sin\alpha\ \cos\beta)$ velocity components.

In addition, another Pitot-static probe was located in the test section inlet to measure the free-stream velocity. The turbulent intensity at the test section inlet was also measured with a hot wire. Finally, the barometric pressure and temperature of the air at the test section inlet were recorded with a data-logger (SD700, Extech Instruments, Nashua, NH, USA), which was used to determine the fluid properties (e.g., density, kinematic viscosity). The signals were sampled at 1000 Hz via an analog data acquisition module (NI-9220, National Instruments, Austin, TX, USA) and chassis (cDAQ-9188, National Instruments, Austin, TX, USA). A commercial software package (LabView, National Instruments, Austin, TX, USA) created a Virtual Instrument (VI) that was used to handle the data with the mean voltage from every 100 samples recorded, which produced an effective sample rate of 10 Hz. The pressure and temperature data-logger did not have an external output, so that data was manually inputted into the VI.

The vertical spacing of the velocity profiles within the wake was 3.18 mm, which was half the diameter of the probe head. Integration of the streamwise velocity is a well-established method for obtaining the total drag on 2D objects that can be extended to 3D models [30]. Three-dimensional considerations were required due to some of the sBFS producing significant coherent structures that persisted into the far-wake region where the wake survey was acquired. A brief overview of the drag analysis is provided here for completeness as well as its relationship to the measurement uncertainty. Assuming a uniform inlet velocity and nearly horizontal streamlines sufficiently far from the model, integration of the streamwise component of velocity in the wake gives the drag coefficient $\left(C_d = D/0.5\rho U_\infty^2 A\right)$ as

$$C_d = \frac{2}{c}\int \frac{U}{U_\infty}\left(1 - \frac{U}{U_\infty}\right)dz.$$

Here, D is the total drag, A is the planform area, U_∞ is the freestream speed, ρ is the fluid density, c is the chord length, z is the vertical distance, and U is the mean streamwise velocity in the wake. The vertical wake velocity profiles were integrated using the trapezoidal rule to determine C_d. No correction for blockage was performed since the maximum solid body blockage was 7%, and for the majority of conditions tested it was below 5%. Corrections for measurements within the wake of a streamlined body are minimal prior to separation [31]. The uncertainty of C_d calculation was determined using standard propagation of uncertainty procedures. While the uncertainty for instruments and geometric measurements were readily available, the final uncertainty was heavily dependent on the covariance between the mean velocity measurements and the free-stream speed. With a covariance of 0.395, the resulting uncertainty in C_d was 3.6% at the maximum test speed. Given the uncertainty of the covariance and weak variation between operation conditions, error bars on C_d plots have been fixed at 5% for reference.

Due to the observation of coherent structures in the far-wake region for a subset of conditions, the induced vorticity within the wake was computed as a measure of the strength of the coherent structures produced by the sBFS. Vorticity is defined as the curl of the flow velocity vector,

$$\vec{\omega} \equiv \nabla \times \vec{V} = \left(\frac{\partial w}{\partial y} - \frac{\partial v}{\partial z}\right)\hat{e}_x + \left(\frac{\partial u}{\partial z} - \frac{\partial w}{\partial x}\right)\hat{e}_y + \left(\frac{\partial v}{\partial x} - \frac{\partial u}{\partial y}\right)\hat{e}_z$$

Since the traverse system could not move in the streamwise direction, none of the streamwise gradients could be computed experimentally. Preliminary results from the computational study indicate that the streamwise component of vorticity (ω_x) is dominant [19]. This is also consistent with the expectation that a coherent structure persisting to the far-field would have significantly stronger gradients in the cross-stream directions relative to the streamwise. Note that since the vorticity is dependent on resolving the velocity vector, only the subset of conditions that used the 5-hole probe could analyze the vorticity. The streamwise vorticity was calculated at each measurement location and then averaged to create vorticity profiles of the wake deficit for each test configuration.

2.1.4. Test Conditions

The airfoil configurations were tested at free-stream speeds of 20 m/s and 26 m/s, which have a corresponding chord length-based Reynolds number $(Re = cU_\infty/\nu)$ of nominally 2.3×10^5 and 3.0×10^5, respectively. The current study focuses on the $Re = 3.0 \times 10^5$ results since no significant variation was observed between test speeds. This was expected due to the relatively narrow Reynolds number range but tested to confirm the insensitivity to Reynolds number over this range. For each test configuration, the angle of attack (α) was typically varied between 0 and 10 degrees in 2-degree increments. The test model configurations were clean wing (i.e., no film), three BFS, and four sBFS (see Table 1 for geometries and locations). For all configurations, the vertical increment (Δz) for the wake survey was 3.18 mm, which was half of the probe head diameter. For the clean wing and 7 BFS configurations, the spanwise increment (Δy) was increased to 25 mm since there was negligible spanwise variation. Conversely, the sBFS configurations produced coherent structures that created spanwise variations; the spanwise increment was reduced to 12.5 mm. In addition, the measurement locations with the sBFS were selected such that measurements were acquired directly downstream of peaks and valleys. The subset of conditions tested with the 5-hole probe were clean wing, BFS at 10% chord, BFS at 44% chord, and sBFS-V1.

2.2. Computational Methods

STAR-CCM+ v2022.1.1, a commercially available CFD software, was used for the computational study. The complex 3D models were created in SolidWorks and imported to STAR-CCM+, which has its own built in 3D-CAD, where the models were further edited to facilitate the simulation. STAR-CCM+ provides built-in automated mesh capabilities that include tetrahedral, trimmer, and polyhedral unstructured meshes. These mesh algorithms also have the capability of utilizing prism layers, which is essential in resolving the near-wall region of a boundary layer. STAR-CCM+ also has the capability to run a large range of physics- and flow-specific models that include RANS, DES, LES, and qDNS, with sub models for each. For the current study, RANS, or Reynolds-Averaged Navier–Stokes equations, which are often used to study the mean characteristics of the flow, were chosen.

The experimental setup was replicated in the computational model. A 3D rectangular domain was created for all simulations. The side walls were given periodic boundary conditions, while the top and bottom walls were subjected to slip conditions. The inlet was a velocity inlet, while the outlet was treated as a pressure outlet. The side walls had periodic boundary conditions. The domain total length was 3.75 m, width 15.24 (width of 3 sBFS), and the height was 0.91 m to match the height of the wind tunnel in the experimental study. In this study, the span of the airfoil was reduced to 3 sBFS widths (152.4 mm). The sBFS-V1 configuration was chosen since it provided the most significant wake structures. The length, width, and thickness were 69.9 mm, 50.8 mm, and 1.1 mm, respectively, with the valley and peak locations at 10% and 45%, respectively. The turbulence model used for this study was k-omega turbulence and the turbulent intensity at the inlet was set to 1%. Surface, polyhedral and prism layer meshers were chosen for this study. The mesh was compared by studying 3 independent meshes comprising 2.5, 14, and 25 million cells. All 3 meshes produced similar results and the one with the highest number of cells was used for all of the analysis.

3. Results

3.1. Experimental Investigation

3.1.1. Reference Conditions

The clean wing (i.e., no step) and BFS configurations were tested as reference conditions for comparison with the sBFS results. The contour plot of the streamwise velocity scaled by the local free-stream speed (U_∞) for the clean wing is shown in Figure 3a with the abscissa the spanwise location (y) and the ordinate the vertical location (z) scaled by the wake half-deficit height $(z_{0.5})$. The wake half-deficit height is the distance from the wake center (i.e., maximum wake deficit) to the location where the wake deficit is half of the maximum deficit. For the current study, it was determined from the average half-deficit height from each spanwise location. This shows that there was a slight spanwise slope observed in the wake survey. Upon inspection, this was determined to be created by a slight misalignment between traverse coordinate system and the test section coordinate system, which, in the analysis, could be corrected by aligning the maximum wake deficit at a given spanwise location. Accounting for the slope, there was no significant spanwise variation in the wake deficit for the clean wing. In addition, this showed that the wake velocity at the maximum wake deficit was nominally 92% of the free-stream speed. This was consistent with wake deficits from streamlined bodies and supports the previous comment that wake corrections for streamlined bodies are minimal [31]. The coefficient of drag (C_d) was then calculated by integrating the wake profiles and averaging the results from individual spanwise locations. The clean wing results were compared with the XFOIL results [32] in Figure 3b. The current C_d results matched within the measurement uncertainty of the theoretical XFOIL results at lower angles of attack. At higher angles of attack, the experimental and XFOIL results appeared to deviate, but the discrepancy was close to the stall angle (10.25 degrees) for this airfoil shape.

The contour plots for the BFS configurations are not shown since there was no spanwise variation observed, but BFS contour plots are presented in the work of KC et al. [29] and KC [33]. The BFS wake structures were similar to that observed on the clean wing in Figure 3a. While the BFS structure was similar, the coefficient of drag was significantly increased relative to the clean wing. The BFS C_d at a chord length of 10%, 27%, and 45% are compared with the clean wing (CW) results in Figure 4. This illustrates the negative impact on the drag performance with the presence of BFS. This is consistent with the literature [34]. The BFS at 27% and 45% chord length produced similar curves to that of the clean wing with an average increase of 33% and 24% increase in C_d, respectively. The curve for BFS at 10% had a different trend, but the generally the C_d decreased with increased chord position. The BFS 10% chord produced the most amount of drag in comparison to BFS at 27 and 45% chord. This is due to the fact that the early step location caused the flow to separate earlier on the airfoil.

The streamwise vorticity (ω_x) was also computed for the clean wing and two of the BFS conditions (10% and 45% chord length), which were selected as reference conditions to align with the peak and valley locations of sBFS-V1. Figure 5 shows the maximum streamwise vorticity in the far-wake region for the clean wing and two BFS configurations. The maximum vorticity was identified from the magnitude of the streamwise vorticity computed within the wake for each test configuration. The general trend for both the clean wing and the BFSs has the maximum vorticity decreased with an increasing angle of attack at small angles. Then, at higher angles of attack, the maximum vorticity begins to increase with increasing the angle of attack. This trend is comparable to that reported in the literature [35]. The clean wing and BFS at 45% have similar trends and magnitudes over the range of angles of attack tested, but BFS at 10% has significantly lower maximum vorticity and the change in trend occurs at a lower angle of attack. This is indicative of a structural change in the flow pattern at BFS of 10% relative to the other reference conditions, which is consistent with the C_d results.

3.1.2. sBFS Conditions

The coefficient of drag (C_d) for all four sBFS configurations is plotted in Figure 6 along with the clean wing and BFS at 10% chord length for reference. The coefficient of drag at zero angle of attack was within the measurement uncertainty for all four sBFS configurations. The sBFS at $\alpha = 0^\circ$ was higher than the clean wing but lower than the BFS at 10% chord, and, of note, sBFS-V1, -V2, and -V4 had the valley located at the 10% chord. At higher angles of attack, the C_d increases except for sBFS-V3, which is nearly constant over the range tested. Since sBFS-V3 was the only configuration with the valley location further downstream than the 10% chord length, this suggests that the drag performance at higher angles of attack might converge to the performance of a BFS at the valley location. The other three sBFS configurations (sBFS-V1, -V2, and -V4) steadily increased C_d with increasing α until 10°, when the value exceeds that of the BFS at 10% chord length. This is consistent with the literature (e.g., [34]), which shows that the location of the step has a significant impact on performance, with reduced impact as the step moves towards the trailing edge. For these cases, the flow separated early compared to when the valley was located further downstream as in the case of sBFS-V3. The early separation caused the drag of the three configurations to rise quickly relative to the sBFS-V3. A comparison between sBFS-V1 and -V2 (i.e., half the length and width of -V1 with same step height) showed that the variation was comparable to the measurement uncertainty until the highest angle of attack. Conversely, when the length-to-width ratio was increased for sBFS-V4, it shows a decrease in C_d for low angles of attack, but then converged to sBFS-V1 and -V2 at higher angles of attack.

Figure 7 compares the velocity contour plots of clean wing, BFS at 10% chord length, and sBFS-V1. Like Figure 3a, the ordinate in Figure 7 is the vertical distance (z) from the wake center scaled by the wake half-deficit ($z_{0.5}$), but the spanwise location (y) is scaled by the sBFS-V1 width (W). As expected, the clean wing and BFS distributions do not show any significant spanwise variation in the deficit. However, the sBFS profile shows a clear spanwise variation in the velocity distribution. This suggests that the sBFS promotes the formation of coherent structures. The streamwise velocity is scaled by the free-stream speed (U_∞), while the other velocity components (v and w) are normalized by their respective maximum magnitudes. The spanwise variation observed for the sBFS-V1 configuration is proportional to the width of the sBFS. This was unexpected since these measurements were acquired five chord lengths downstream of the model. The sBFS-V1 coherent structures are apparent in all three velocity components with a scale that is nominally twice the wake deficit's half height ($z_{0.5}$). This is because the coherent structures are turbulent, which will have a three-dimensional flow field. The cross-stream components indicate that the structures form in counter-rotating pairs.

The vorticity within the wake was computed to quantify the sBFS-V1's coherent structure production. The maximum streamwise vorticity of the sBFS-V1 configuration is compared with that of the clean wing and BFS at 10% chord length in Figure 8. As expected, the vorticity is consistently higher for sBFS-V1 relative to both the clean wing and the 10% chord BFS. This is especially true at zero angle of attack where the maximum streamwise vorticity was 2.7 and 3.5 times larger than the clean wing and 10% chord BFS, respectively. This suggests that these low-profile shapes are imparting significant rotation that can redistribute the momentum on the airfoil surface, which is critical for passive flow control.

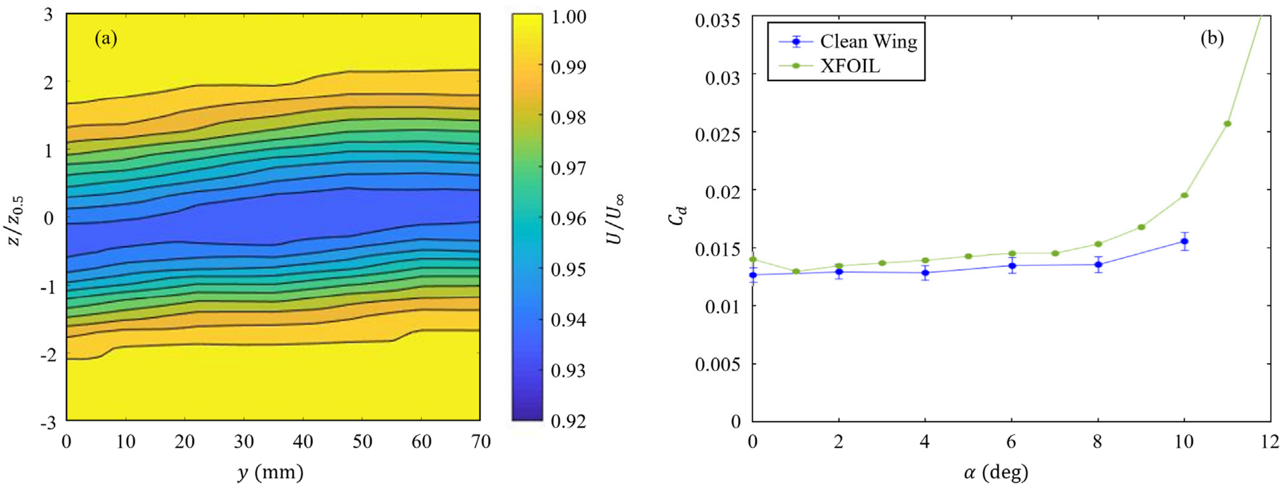

Figure 3. (**a**) Clean wing contour plot of wake at Reynolds number of 300,000. (**b**) Coefficient of drag (C_d) versus angle of attack for the clean wing compared with estimation using XFOIL.

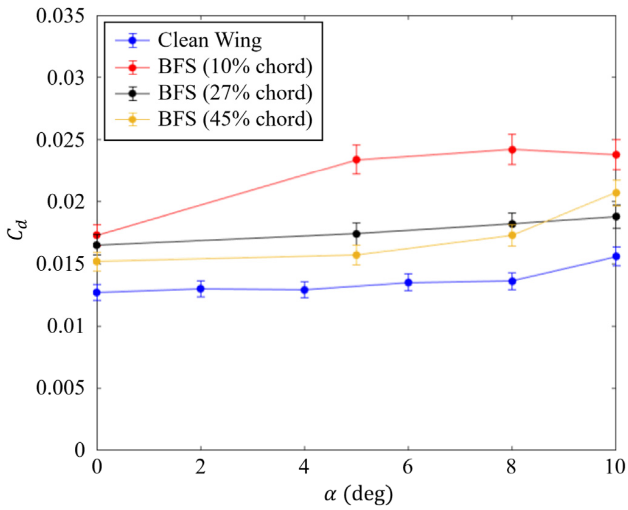

Figure 4. BFS coefficient of drag as function of angle of attack and chord position compared to the clean wing.

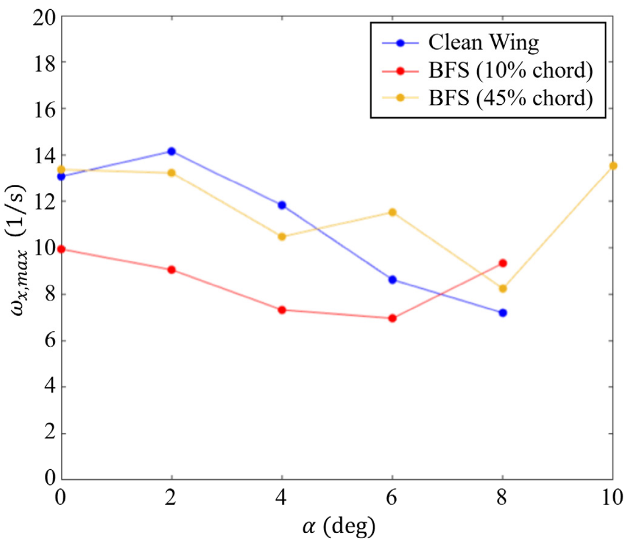

Figure 5. The maximum streamwise vorticity (ω_x) for the clean wing and BFS configurations tested with the five-hole probe.

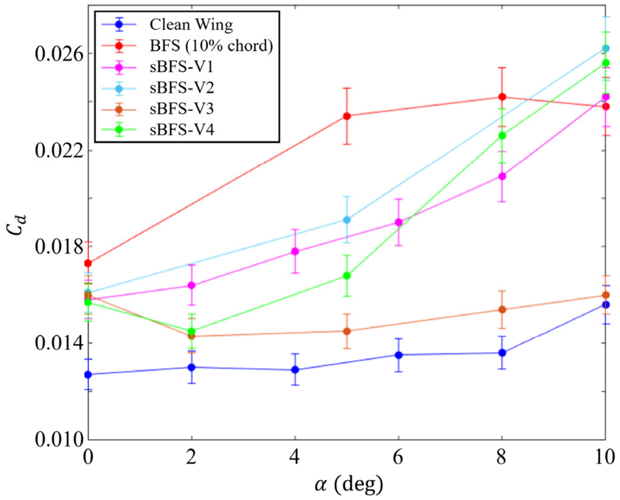

Figure 6. The coefficient of drag for all sBFS configurations tested as a function of the angle of attack. Curves for the clean wing and BFS at 10% chord are included for reference.

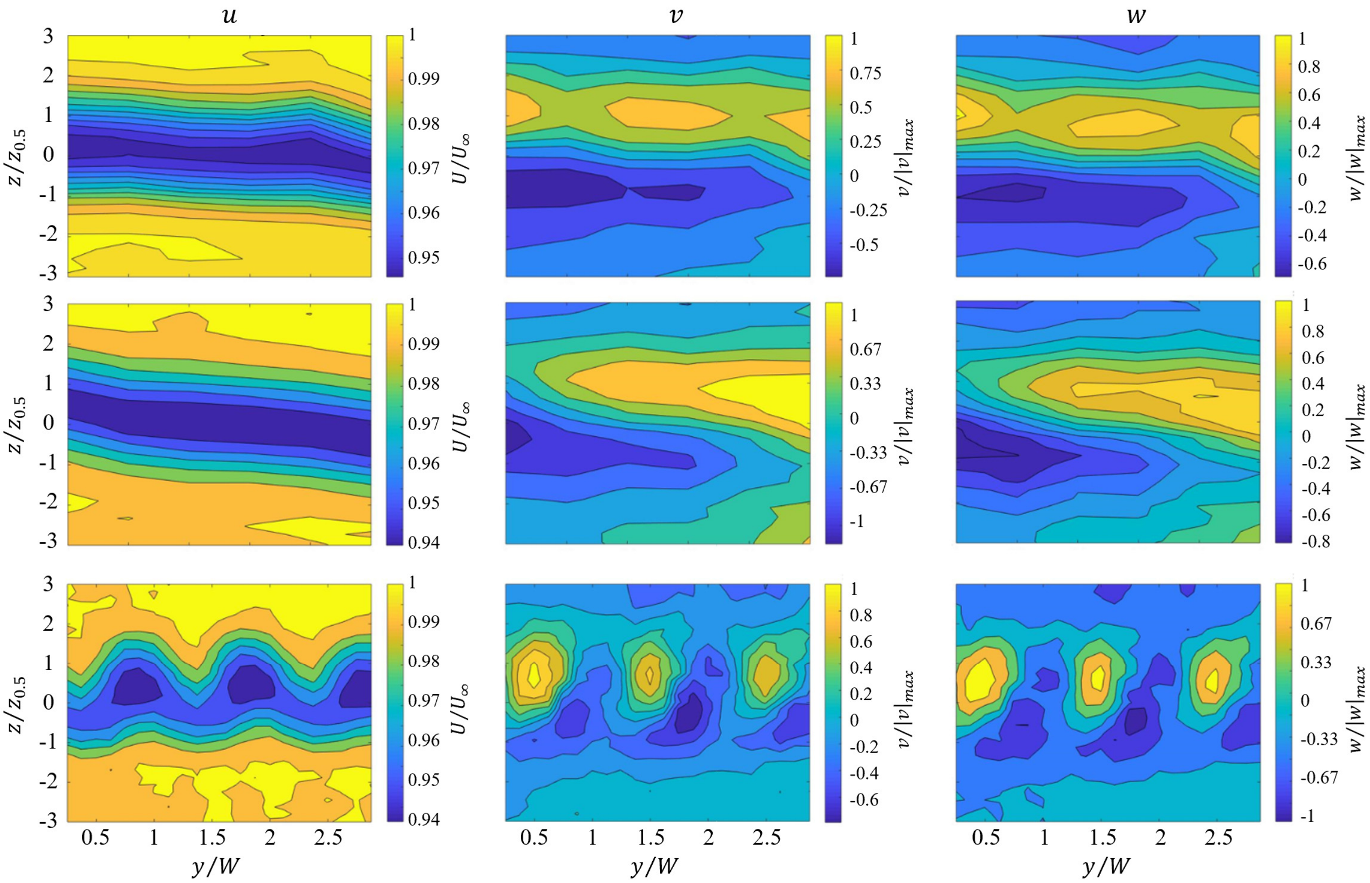

Figure 7. Contour plots of the (**left column**) streamwise, (**middle column**) spanwise, and (**right column**) vertical velocity components from the (**top row**) clean wing, (**middle row**) BFS at 10% chord length, and (**bottom row**) sBFS-V1.

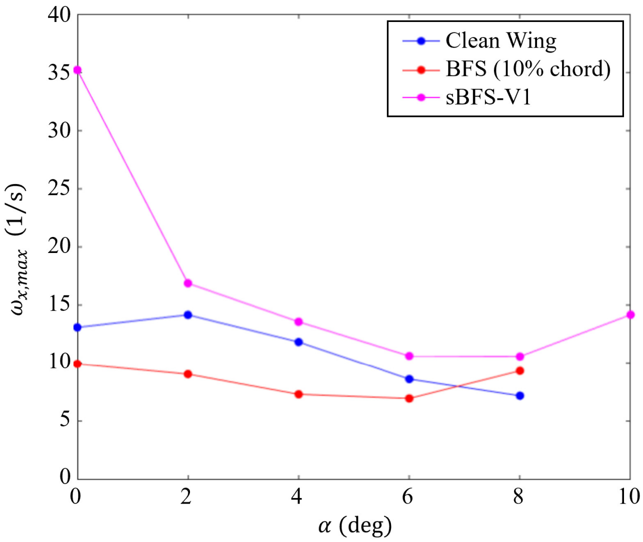

Figure 8. Maximum streamwise vorticity for the sBFS-V1 configuration compared with the clean wing and 10% chord BFS.

3.2. Computational Investigation

The experimental results provided insights into the overall impact on the airfoil's performance, but the specific flow modifications induced by the sBFS could not be examined. Consequently, a computational model was also developed and validated via direct comparison of the available experimental data with the computational results. The comparison between the experimental and computational wake results for the sBFS-V1 condition are shown in Figure 9. The experimental result is the streamwise component in the lower row of Figure 7. The peaks and the valleys of the sBFS are well aligned with the structures in the wake region, which is also observed in the computational results. The size and pattern of the structures are in excellent agreement. The velocity magnitudes, indicated by the color, are also in agreement with each other. Thus, giving confidence that the computational model is providing an accurate representation of the experimental flow field.

Now, the induced vorticity in the far-wake region can be explored with the full velocity gradient distribution available. The streamwise vorticity in the far-wake region from the computational simulation is shown in Figure 10. The resulting structures are consistent with the experimental results. This shows that the coherent structure in the far-wake region is counter-rotating pairs. This also shows that the counter-rotating vortices are not symmetric, with the red vortices showing a much tighter core (i.e., darker color) relative to the blue vortices. This is also consistent with the experimental observations.

Now, the computational model can be utilized to examine the flow field induced by the sBFS on the airfoil. Streamlines were used to explore the flow patterns induced by the sBFS. This revealed that streamlines originate from near the wall prior to the step rollup as they go over the step. Near-surface streamlines near the sBFS valley location are then redirected from the streamwise direction towards the sBFS peak. Conversely, the streamlines that originate in the far-wall region do not have any significant spanwise movement. These differences are illustrated in Figure 11, where half of the streamlines originate from near the surface and the other half in the far-wall region. In addition, Video S1 in the Supplemental Material shows the computational simulation streamlines from various views and their relationship to the resulting wake structure. In addition, Video S1 shows that the region directly downstream of the peak has flow reversal, which is indicative of flow separation. Conversely, the flow remains attached to the trailing edge in the region directly downstream of the valley. Thus, it was concluded that the near-surface flow becomes entrained in the direction towards the peak and this is responsible for producing the coherent structures that persist into the far-wake region. This finding is consistent with the work of Wang et al. [36]

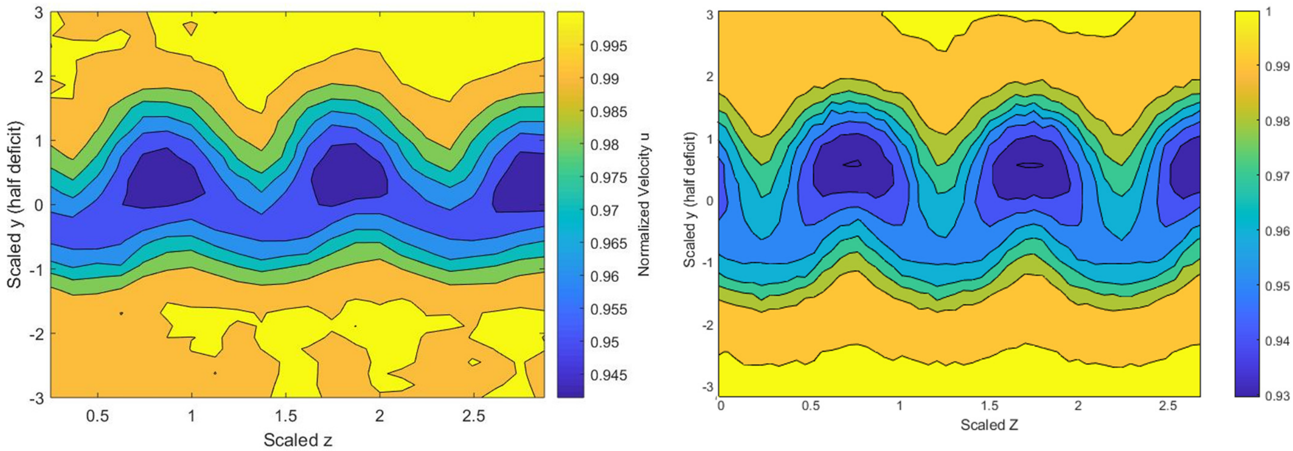

Figure 9. Comparison of the streamwise velocity contour plots produced by the (**left**) experimental measurements and (**right**) computational models.

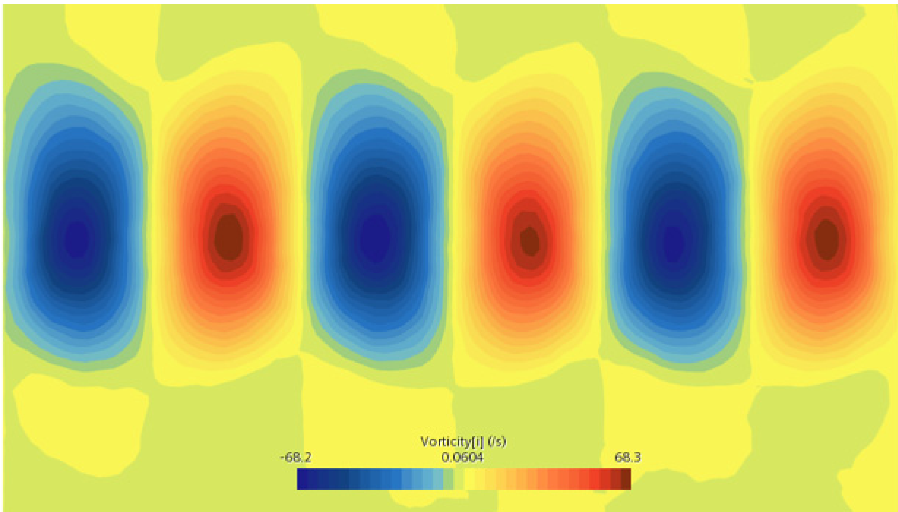

Figure 10. Computational simulation results of the streamwise vorticity in the far-wake region from the sBFS-V1 configuration.

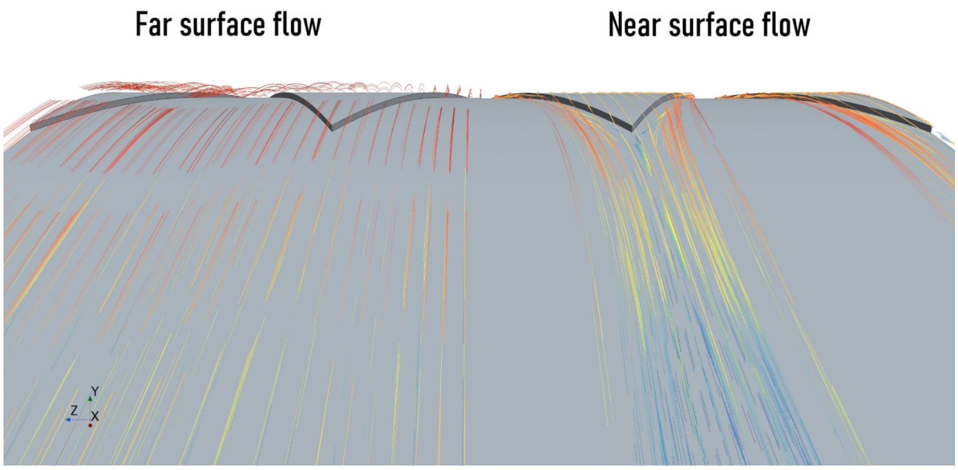

Figure 11. Flow entrainment over the sBFS visualized with streamlines colored based on the local relative speed (cool to warm colors indicate low to high speeds). Streamlines originate from either (**left**) the far-wall or (**right**) near-surface region upstream of the step.

4. Discussion

The lowest drag results for the BFS (i.e., 45% chord) and sBFS are compared along with the clean wing results in Figure 12. As expected, the sBFS did not reduce the drag relative to the clean wing, though at the highest angle of attack tested, the two configurations are within the measurement uncertainty. Conversely, sBFS-V3 had lower drag than BFS at 45% chord for nearly all angles of attack tested, and at zero angle of attack, the increase was comparable to the measurement uncertainty. This was in spite of the fact that sBFS-V3 had the valley location (27% chord) closer to the leading edge than the BFS at 45% chord. Note that the peak location of sBFS-V3 was at 45%, which matches the BFS location compared in Figure 12. As previously discussed, airfoils regularly have BFSs such as that created by the slat step on the wing on the Boeing 737, which is nominally located at the 10% chord length. These results indicate that the sBFS can mitigate the negative drag effect created by BFS. These findings are consistent with recent work studying microsteps, which have shown that they could have a significant impact on boundary layer flows at scales much larger than their step height [37,38]. It should also be noted that minimal effort has been dedicated to date on the sizing of the sBFS relative to the flow parameters, which is critical, as most passive flow-control methods require a tuning of the geometry given the flow parameters.

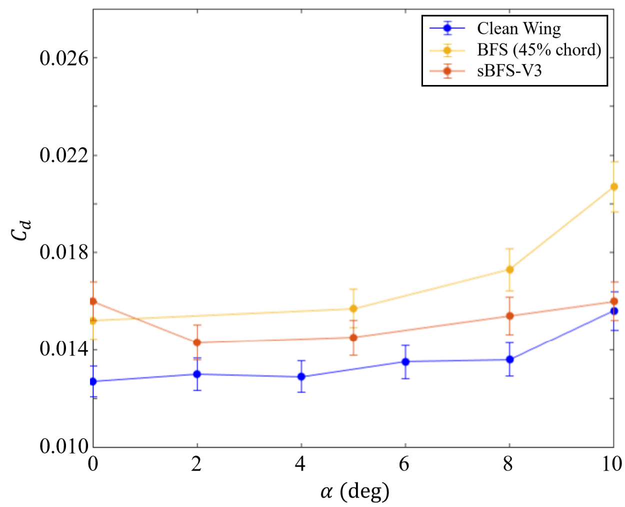

Figure 12. Comparison of the sBFS-V3 that produced the lowest C_d values with that of the clean wing and the BFS with the lowest drag (i.e., BFS at 45% chord length). The sBFS-V3 had the valley and peak at 27% and 45% chord length, respectively.

The computational study showed evidence that these coherent structures are formed by the sBFS redirecting the near-wall flow at the valley towards the peaks. Then, downstream of the valley, the flow remains attached even when the flow separates downstream of the sBFS peak. The pattern then persists downstream, forming the spanwise variation observed in the far-wake region. In addition, the streamwise vorticity in the computational study showed that the coherent structures in the wake are counter-rotating pairs.

5. Conclusions

Wake surveys in the far-wake region of a LA203A airfoil model were used to measure the drag associated with the application of a protective film around the model's leading edge. A BFS was created on the model with a thin film. The use of a serrated (i.e., sawtooth) pattern on the trailing edge of the BFS was explored to investigate its potential for mitigating negative impacts. For reference, the clean wing (i.e., no film) and three standard BFSs were tested. These results showed that the BFS increased the drag relative to the clean wing, and that the drag increased the closer the BFS was to the leading edge. Four sBFS configurations, each with the same step height, were tested. In general, over most angles of attack, the sBFS produced lower drag relative to the BFS located at the sBFS valley location.

In addition, vorticity and contour plots showed that the sBFS produced strong coherent structures that could persist into the far-wake region.

Computational simulations showed that these structures were produced by the sBFS, with the flow near the surface of the airfoil being entrained in the direction of the sBFS peak. This induced motion modified the downstream flow structure, which, in the sBFS condition computationally examined, impacted separation at the trailing edge. This pattern at the trailing edge likely produced such a strong pattern in the far-wake region, though they were induced by the sBFS as evidenced by the structure alignment with the sBFS peak and valley geometry. The strength of the structures does appear to be dependent, in part, on the length-to-width ratio of the sBFS; however, the possible influence of the width itself was not studied and should be explored further in connection with the impact on the trailing edge separation.

Overall, there is evidence that sBFS could mitigate the adverse effects on drag associated with BFS on airfoils, which are frequently created due to the addition of protective leading edge films or mismatch in height between adjoining surfaces. Mitigating these effects could lead to improved performance across certain flight regimes, and improve the efficiency of wind turbines. The next steps are to develop an LES-based simulation to enable a study of the coherent structures on the airfoil and how they are modified by the sBFS; these insights will enable the tuning of the step geometry based on the operation condition.

Supplementary Materials: The following supporting information can be downloaded at: https://www.mdpi.com/article/10.3390/inventions8060160/s1, Video S1: Video of streamlines originating from either the near-wall or far-wall region upstream of the step.

Author Contributions: Conceptualization, R.J.K., B.R.E. and J.D.J.; methodology, R.J.K., N.A.L., B.R.E. and J.D.J.; software, R.J.K., T.C.W. and A.S.A.; validation, R.J.K., T.C.W., A.S.A., J.D.J., B.R.E. and N.A.L.; formal analysis, R.J.K., A.S.A., B.R.E. and N.A.L.; investigation, R.J.K., T.C.W., A.S.A., J.D.J., B.R.E. and N.A.L.; resources, B.R.E. and J.D.J.; data curation, R.J.K., A.S.A. and N.A.L.; writing—original draft preparation, R.J.K., T.C.W., A.S.A., J.D.J., B.R.E. and N.A.L.; writing—review and editing, R.J.K. and B.R.E.; visualization, R.J.K.; supervision, B.R.E. and J.D.J.; project administration, B.R.E. and J.D.J.; funding acquisition, B.R.E. and J.D.J. All authors have read and agreed to the published version of the manuscript.

Funding: This research was funded, in part, by B.R.E.'s John Brammer Professorship.

Data Availability Statement: The data presented in this study are available on request from the corresponding author.

Acknowledgments: The authors thank Kurt Rouser and his laboratory group for their assistance with wind tunnel operations and measurements.

Conflicts of Interest: The authors declare no conflict of interest.

References

1. Hood, M.J. *The Effects of Surface Waviness and of Rib Stitching on Wing Drag*; Technical Report NACA-TN-724; National Advisory Committee for Aeronautics: Washington, DC, USA, 1939.
2. Young, A.D.; Paterson, J.H. *Aircraft Excrescence Drag*; Technical Report AGARD-AG-264; North Atlantic Treaty Organization (NATO) Advisory Group for Aerospace Research and Development (AGARD): Bruxelles, Belgium, 1981.
3. Rizzetta, D.P.; Visbal, M.R. Numerical Simulation of Excrescence Generated Transition. *AIAA J.* **2014**, *52*, 385–397. [CrossRef]
4. Rizzetta, D.P.; Visbal, M.R. Plasma-Based Flow Control for Delay of Excrescence-Generated Transition. *AIAA J.* **2015**, *53*, 1455–1467. [CrossRef]
5. Rizzetta, D.P.; Visbal, M.R. Plasma-Based Control of Transition on a Wing with Leading-Edge Excrescence. *AIAA J.* **2016**, *54*, 129–140. [CrossRef]
6. Rizzetta, D.P.; Visbal, M.R. Plasma-Based Control of Excrescence-Generated Transition on a Swept Wing. *AIAA J.* **2017**, *55*, 1610–1621. [CrossRef]
7. Major, D.; Palacios, J.; Maughmer, M.; Schmitz, S. A numerical model for the analysis of leading-edge protection tapes for wind turbine blades. *J. Phys. Conf. Ser.* **2020**, *1452*, 012058. [CrossRef]
8. Major, D.; Palacios, J.; Maughmer, M.; Schmitz, S. Aerodynamics of leading-edge protection tapes for wind turbine blades. *Wind Eng.* **2021**, *45*, 1296–1316. [CrossRef]

9. Agrim, S.; Sapre, C.A.; Selig, M.S. Effects of leading-edge protection tape on wind turbine blade performance. *Wind Eng.* **2012**, *36*, 525–534.
10. Witherspoon, S.; Finaish, F. Experimental and Computational studies of flow developments around an airfoil with backward-facing steps. In Proceedings of the 14th Applied Aerodynamics Conference, New Orleans, LA, USA, 17–20 June 1996.
11. Kostas, J.; Soria, J.; Chong, M. Particle image velocimetry measurements of a backward-facing step flow. *Exp. Fluids* **2002**, *33*, 838–853. [CrossRef]
12. Barri, M.; Andersson, H.I. Turbulent flow over a backward-facing step. Part 1. Effects of anti-cyclonic system rotation. *J. Fluid Mech.* **2010**, *665*, 382–417. [CrossRef]
13. Hasan, M.A.Z. The flow over a backward-facing step under controlled perturbation: Laminar separation. *J. Fluid Mech.* **1992**, *238*, 73–96. [CrossRef]
14. Lin, J. Control of turbulent boundary-layer separation using micro-vortex generators. In Proceedings of the 30th Fluid Dynamics Conference, Norfolk, VA, USA, 28 June–1 July 1999.
15. Yao, C.; Lin, J.; Allen, B. Flowfield measurement of device-induced embedded streamwise vortex on a flat plate. In Proceedings of the 1st Flow Control Conference, St. Louis, MO, USA, 24–26 June 2002.
16. Storms, B.L.; Jang, C.S. Lift enhancement of an airfoil using a Gurney flap and vortex generators. *J. Aircr.* **1994**, *31*, 542–547. [CrossRef]
17. Lin, J.C. Review of research on low-profile vortex generators to control boundary-layer separation. *Prog. Aerosp. Sci.* **2002**, *38*, 389–420. [CrossRef]
18. Babinsky, H.; Li, Y.; Ford, C.W.P. Microramp control of supersonic oblique shock-wave/boundary-layer interactions. *AIAA J.* **2009**, *47*, 668–675. [CrossRef]
19. Chu, H.B.; Zhang, B.Q.; Chen, Y.C. Controlling flow separation of high lift transport aircraft with micro vortex generators. *J. Northwestern Polytech. Univ.* **2011**, *29*, 799–805.
20. Bolgar, I.; Scharnowski, S.; Kahler, C.J. Passive Flow Control for Reduced Load Dynamics Aft of a Backward-Facing Step. *AIAA J.* **2019**, *57*, 120–131. [CrossRef]
21. Paruchuri, C.; Joseph, P.; Ayton, L.J. On the superior performance of leading edge slits over serrations for the reduction of aerofoil interaction noise. In Proceedings of the 2018 AIAA/CEAS Aeroacoustics Conference, Atlanta, Georgia, 25–29 June 2018; p. 3121.
22. Calvert, M.; Wong, T.-C. Aerodynamic Impacts of Helicopter Blade Erosion Coatings. In Proceedings of the 30th AIAA Applied Aerodynamics Conference, New Orleans, LA, USA, 25–28 June 2012; p. 2914.
23. Scholbrock, A. *Power Performance Results UsingWind Turbine Blade Enhancing Devices Developed By Edge Aerodynamix*; Technical Report; National Renewable Energy Laboratory: Golden, CO, USA, 2017.
24. Wilson, T.C.; KC, R.; Lucido, N.A.; Elbing, B.R.; Alexander, A.S.; Jacob, J.D.; Ireland, P.; Black, J.A. Computational Investigation of the Conformal Vortex Generator. In Proceedings of the AIAA Scitech 2019 Forum, San Diego, CA, USA, 7–11 January 2019. [CrossRef]
25. Kibble, G.A. Experimental and Computational Investigation of the Conformal Vortex Generator. Master's Thesis, Oklahoma State University, Stillwater, OK, USA, 2017.
26. Lucido, N.A.; KC, R.; Wilson, T.C.; Jacob, J.D.; Alexander, A.S.; Elbing, B.R.; Ireland, P.; Black, J.A. Laminar Boundary Layer Scaling Over a Conformal Vortex Generator. In Proceedings of the AIAA Scitech 2019 Forum, San Diego, CA, USA, 7–11 January 2019. [CrossRef]
27. Lucido, N.A. Investigation of Low-Profile Vortex Generators on Low Reynolds Number Propellers for Small Unmanned Aircraft. Master's Thesis, Oklahoma State University, Stillwater, OK, USA, 2019.
28. Zimbelman, T. Plasma Flow Control for Distortion Tolerant Fans with Aircraft Boundary Layer Ingestion. Master's Thesis, Oklahoma State University, Stillwater, OK, USA, May 2018.
29. KC, R.; Lucido, N.A.; Wilson, T.C.; Elbing, B.R.; Jacob, J.D.; Alexander, A.S.; Ireland, P.; Black, J.A. Investigation of Wake Survey over a Wing with Conformal Vortex Generators. In Proceedings of the AIAA Scitech 2019 Forum, San Diego, CA, USA, 7–11 January 2019. [CrossRef]
30. Brune, G.W. Quantitative Low-Speed Wake Surveys. *AIAA J. Aircr.* **1994**, *31*, 249–255. [CrossRef]
31. Maskell, E.C. *A Theory of the Blockage Effects on Bluff Bodes and Stalled Wings in a Closed Wind Tunnel*; Technical Report ARC Reports and Memoranda R&M 3400; Aeronautical Research Council: London, UK, 1963.
32. Drela, M. XFOIL: An Analysis and Design System for Low Reynolds Number Airfoils. In *Low Reynolds Number Aerodynamics*; Mueller, T.J., Ed.; Springer: Berlin/Heidelberg, Germany, 1989; pp. 1–12. [CrossRef]
33. KC, R.J. Investigation of Low-Profile Vortex Generators via Experimental Methods. Master's Thesis, Oklahoma State University, Stillwater, OK, USA, July 2019.
34. Mishriky, F.; Walsh, P. Effect of the backward-facing step location on the aerodynamics of a morphing wing. *Aerospace* **2016**, *3*, 25. [CrossRef]

35. Wendt, B.J. Parametric study of vortices shed from airfoil vortex generators. *AIAA J.* **2004**, *42*, 2185–2195. [CrossRef]
36. Wang, B.; Liu, W.D.; Sun, M.B.; Zhao, Y.X. Fluid redistribution in the turbulent boundary layer under the microramp control. *AIAA J.* **2015**, *53*, 3777–3787. [CrossRef]
37. Falco, R. Drag Reduction Method and Surface. US Patent 5,133,519, 28 July 1992.
38. Al-Jaburi, K.; Feszty, D. Passive Flow Control of Dynamic Stall via Surface-Based Trapped Vortex Generators. *J. Am. Helicopter Soc.* **2018**, *63*, 1–14. [CrossRef]